Acta Pharmaceutica Sinica B 2026;16(2):1059−1073

Chinese Pharmaceutical Association
Institute of Materia Medica, Chinese Academy of Medical Sciences

Acta Pharmaceutica Sinica B

www.elsevier.com/locate/apsb
www.sciencedirect.com

ORIGINAL ARTICLE

An immunostimulant nanomedicine enhances radioimmunotherapy by remodeling the tumor immunosuppressive landscape after radiotherapy

Mengwan Jiang[a,*,†], Mingyue Chen[b,†], Wen Zou[c], Yingxin Xie[c], Jinjin Shi[c,*], Junjie Liu[c,*], Aibing Chen[b,*], Xiu Zhao[c,*]

[a]*School of Artificial Intelligence and Big Data, Henan University of Technology, Zhengzhou 450001, China*
[b]*College of Chemical and Pharmaceutical Engineering, Hebei University of Science and Technology, Shijiazhuang 050018, China*
[c]*School of Pharmaceutical Sciences, Zhengzhou University, Zhengzhou 450001, China*

Received 5 May 2025; received in revised form 30 July 2025; accepted 2 October 2025

KEY WORDS

Radiotherapy;
Breast cancer;
Immune landscape;
Myeloid-derived suppressor cells;
Apoptosis;
Pyroptosis;
Nanomedicine;
Tumor microenvironment

Abstract Studies have shown that radiotherapy (RT) has powerful immune-stimulating effects. However, RT-mediated distal tumor regression is rare in clinical practice. Here, with an animal experimental model, we found that RT shaped an immunosuppressive landscape characterized by a high-influx of myeloid-derived suppressor cells (MDSCs), and the induction of immunologically silent tumor apoptosis, hindering the efficacy of radioimmunotherapy. To address this issue, we developed a spatiotemporally controlled nanomedicine for remodeling the immunosuppressive tumor microenvironment (TME) post-RT. Decitabine (DAC)-loaded ferritin (Ft) were crosslinked *via* an azobenzene linker, and meanwhile encapsulated with all-trans retinoic acid (ATRA) to construct a Ft@DAC@ATRA nanoassembly (denoted as FD@ATRA), which dissociated into monodispersive Ft@DAC units in hypoxia TME. The released ATRA could eliminate immunosuppressive MDSCs, and meanwhile Ft@DAC selectively induced immunogenic pyroptosis of the tumor by targeting the transferrin receptor 1 overexpressed on the tumor to effectively activate $CD8^+$ T cells. FD@ATRA treatment reshaped the tumor immune landscape post-RT with an increase of 16.8% in tumor-infiltrating IFN-γ^+CD8^+ T cells. Moreover, FD@ATRA-

*Corresponding authors.
E-mail addresses: shijinyxy@zzu.edu.cn (Jinjin Shi), liujunjie@zzu.edu.cn (Junjie Liu), chen_ab@163.com (Aibing Chen), zhaoxiu@zzu.edu.cn (Xiu Zhao), jiangmw@haut.edu.cn (Mengwan Jiang).
†These authors made equal contributions to this work.
Peer review under the responsibility of Chinese Pharmaceutical Association and Institute of Materia Medica, Chinese Academy of Medical Sciences.

https://doi.org/10.1016/j.apsb.2025.11.012

enhanced RT remained effective in large, treatment-resistant tumors, and the inhibition rate of FD@ATRA-enhanced RT on distant tumors improved by 47% compared to the RT group alone, providing an effective therapeutic approach to improve the clinical outcomes of radioimmunotherapy.

1. Introduction

Radiotherapy (RT) is employed in the treatment of approximately 50% of patients with cancer, which can reduce tumor burden by inducing DNA damage[1-3]. Recently, mounting evidence has revealed that RT has robust immunostimulatory effects. Mechanistically, RT can enhance neoantigen expression, enriching the peptide repertoire for effector T cell recognition and antitumor immune activation[4,5]. In addition, the released double-stranded DNA (dsDNA) into the cytoplasm after RT can activate cyclic GMP−AMP synthase (cGAS)-stimulator of interferon genes (STING) pathway-mediated innate immunity[6-8]. RT-activated systemic immune responses are beneficial for reducing radiation dose and inhibiting tumor recurrence. For example, it was reported that compared with immuno-competent mice, the radiation dose necessary to facilitate tumor regression was 1.7-fold higher in immune-deficient mice[9]. Unfortunately, RT-mediated distal tumor regression is uncommon in clinical practice, only a small subset of patients show a response to radioimmunotherapy[10-12]. Thus, to enhance the efficiency of radioimmunotherapy in the clinic, a more complete understanding of the interaction of RT and antitumor immunity in pre-clinical models can reveal new strategies.

Emerging evidence has shown that, in addition to the enhanced antitumor immune response by activating cytotoxic T lymphocytes[13-16], RT can also promote the infiltration of some immunosuppressive cells, including regulatory T cells, tumor-associated macrophages (TAMs) and myeloid-derived suppressor cells (MDSCs)[17-20], which complicates the interpretation of the immune landscape in patients receiving radiotherapy. Currently, various therapeutic strategies targeting the immunosuppressive environment have been developed to enhance radioimmunotherapy[21-27], however, the therapeutic effect is still limited. The attempts to reveal and inhibit the underlying principles responsible for radiotherapy-modulated immunosuppressive effects are highly required for improved patient outcomes.

Here, with an animal experimental model, we found that RT slightly inhibited tumor growth after irradiation, and the treatment benefits of RT hadn't been significantly improved when combined with α-PD-L1. Further transcriptomic analysis combined with flow cytometry revealed that RT shaped an immunosuppressive landscape characterized by a high-influx of $CD45^+$ immune cells, with the majority being immunosuppressive MDSCs. MDSCs are a group of heterogenous immature myeloid cells with potent immune suppressive functions[28-30]. Additionally, as reported in most literature, we observed that RT induced immunologically silent tumor apoptosis, which greatly weakened the recognition of tumor cells by $CD8^+$ T cells[31-32]. Based on RT-induced immunosuppressive principles, we developed a tumor microenvironment (TME) responsive immunomodulator to enhance its systemic antitumor immune responses. Decitabine (DAC), a DNA methyltransferase inhibitor, was encapsulated into the cavity of ferritin (Ft) with good biocompatibility. The obtained Ft@DAC was then crosslinked *via* a hypoxia-responsive azobenzene linker, and meanwhile all-trans retinoic acid (ATRA) was encapsulated to obtain FD@ATRA nanoassembly (Scheme 1A). FD@ATRA could be dissociated under hypoxic tumor microenvironment to enable on-demand release of ATRA and tumor-targeted DAC delivery. DAC induced immunogenic tumor pyroptosis by upregulating gasdermin E (GSDME) protein and released abundant antigens to activate $CD8^+$ T cells, while ATRA eliminated immunosuppressive MDSCs, reprogramming the post-RT immunosuppressive TME into an immunogenic phenotype (Scheme 1B). Notably, compared with RT group alone, the frequency of tumor-infiltrating IFN-γ^+CD8^+ T cells and $Ki67^+CD8^+$ T cells in RT+FD@ATRA group significantly increased by 16.8% and 19.4%, respectively, thus effectively facilitating regression of primary and distal tumors when combined with PD-L1 blockade. Moreover, FD@ATRA remained effective in large, treatment-resistant tumors. This work holds a promising strategy for improving the clinical benefits of radioimmunotherapy by reshaping the tumor immune landscape after RT.

2. Material and methods

2.1. Materials

Ferritin was purchased from Sigma-Aldrich (USA). Decitabine (DAC) was obtained from Aladdin (China). All-*trans* retinoic acid (ATRA) and Red blood cell lysis were purchased from Solarbio (China). Azobenzene-4,4-dicarboxylic acid (AZO) was purchased from Shanghai Yuanye (China). *InVivo*MAb anti-mouse PD-L1 was purchased from Bioxcell (USA). The Annexin V-FITC/PI Apoptosis assay Kit and Lactate dehydrogenase cytotoxicity test kit were purchased from Shanghai Beyotime (China). Mouse ATP ELISA detection kit, Mouse Interleukin-1β (IL-1β) ELISA detection kit, Mouse Interleukin-6 (IL-6) Kit, Mouse Interleukin-12 (IL-12) Kit, Mouse Tumor Necrosis Factor-alpha (TNF-α) Kit were obtained from Shanghai Mlbio (China). Mouse Adenosine Enzyme Linked Immunoassay Kit was purchased from PYRAM (China). APC-Cy7 anti-mouse CD45, PE/Cy5 anti-mouse CD11b, FITC anti-mouse CD3a, APC/Cy7 anti-mouse CD8a, APC anti-mouse IFN-γ, PE anti-mouse Ki67 were obtained from Biolegend (USA). Cytofix Fix Buffer and Perm/Wash Buffer were purchased from BD Biosciences (USA). The Tumor Dissociation Kit (mouse) was purchased from Miltenyi (GER).

2.2. Mice

Female BALB/c mice (18−20 g) were purchased from Beijing Speiford Biotechnology Co., Ltd. (Beijing). The license number is SCXK (jing) 2019-0110. All experimental procedures were

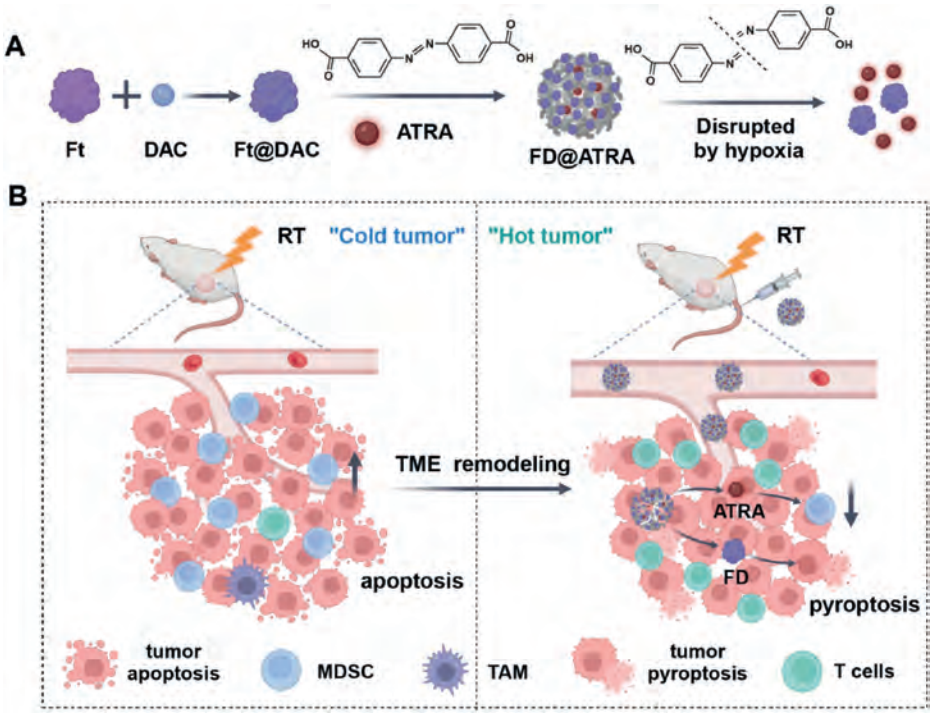

Scheme 1 Schematic illustration of immunomodulatory nanomedicine for enhanced radioimmunotherapy by reshaping the tumor immune landscape after radiotherapy. (A) Illustration of the synthetic procedure for FD@ATRA. (B) Radiotherapy (RT) shaped an immunosuppressive landscape marked by a high-influx of myeloid-derived suppressor cells (MDSCs) and the induction of immunologically silent tumor apoptosis. The tumor microenvironment (TME)-activatable FD@ATRA nanoassembly could dissociate into monodispersive Ft@DAC unit in hypoxia TME, enabling spatiotemporally controlled ATRA and DAC delivery to MDSCs and tumor cells, respectively. FD@ATRA cooperatively remodeled the immunosuppressive TME post-RT by inducing immunogenic tumor pyroptosis and meanwhile eliminating immunosuppressive MDSCs to effectively activate $CD8^+$ T cells for improving the treatment benefits of radioimmunotherapy.

executed according to the protocols approved by the Zhengzhou University Animal Care and Use Committee.

2.3. *Construction of mouse breast cancer model*

4T1 breast cancer cells in the logarithmic growth phase were collected and re-suspended in PBS. The re-suspended cell suspension (100 μL, 2×10^6) was subcutaneously injected into BALB/c mice. After successful inoculation, the survival status of the mice was observed, and the tumor volume was measured.

2.4. *Detection of the anti-tumor activity of RT and RT in combination with α-PD-L1*

When the tumor volume of tumor-bearing mice grew to 80 mm^3, the mice with similar weight were randomly divided into the Saline group and RT group, with six mice in each group. The tumor tissue of mice in the RT group was treated with 6 Gy irradiation (Precision X-Ray, USA), other parts of the mice were covered with lead blocks during irradiation. To further study the antitumor effect of RT in combination with α-PD-L1, tumor-bearing mice were randomly divided into RT group and RT+α-PD-L1 group, with six mice in each group. The tumor tissues of tumor-bearing mice in each group were irradiated with 6 Gy, and the mice in the RT+α-PD-L1 group were intraperitoneally injected with α-PD-L1 (5 mg/kg) at 12 h post-irradiation, the tumor volume and survival status of the mice was monitored every two days.

2.5. *Transcriptome analysis of tumor tissue after RT*

After 48 h of RT treatment, the tumor tissues of mice in the saline and RT groups were collected in a sterile and enzyme-free environment, cleaned with sterile water, quick-frozen in liquid nitrogen, and stored at −80 °C for transcriptome analysis.

2.6. *Flow cytometry analysis of immune cell phenotype in tumor tissue after RT*

To further determine the infiltration of immune cells in the tumor microenvironment after radiotherapy, the tumor tissues of mice in the saline and RT groups were collected at 48 h post-RT treatment, and the single cell suspension was prepared according to instructions of Tumor Dissociation Kit. APC-Cy7 anti-mouse CD45, PE/Cy5 anti-mouse CD11b, PE anti-mouse Ly-6G and Ly-6C were added to the cell suspension to detect the infiltration of MDSCs in tumor tissues.

2.7. *Preparation of Ft@DAC*

7.5 mg of DAC and 2.5 mg of Ft were accurately weighed and subsequently dissolved in 2 mL of ultrapure water, respectively. The above two solutions were mixed in a round bottom flask and then reacted at 60 °C for 90 min at a stir speed of 2000 rpm (DLAB Scientific Co., Ltd., China). The obtained product was centrifuged using an ultrafiltration centrifuge tube (Merck Millipore, Germany) to remove free DAC and obtain Ft@DAC.

2.8. Preparation of Ft@DAC@ATRA (FD@ATRA)

1.7 mg of EDC, 0.9 mg of NHS, and 1.6 mg of AZO were accurately weighed and solved in 400 μL of dimethyl sulfoxide (DMSO), respectively. The above three solutions were mixed by ultrasound and reacted at room temperature for 2 h. Subsequently, ATRA (6 mg) was dissolved in 500 μL of DMSO under dark conditions. AZO and ATRA solutions were dropwise added to the obtained Ft@DAC in PBS solution, after reaction for 12 h, the final product was purified using a dialysis membrane with a molecular weight of 3500 KD to obtain FD@ATRA.

2.9. Detection of ATRA release under normoxia and hypoxia conditions

$Na_2S_2O_4$ was applied to simulate the hypoxia environment. First, FD@ATRA was dispersed in PBS containing 2 mmol/L $Na_2S_2O_4$, and then the mixed solution was placed in a dialysis bag with a molecular weight of 3500 kD. 2 mL of dialysate at the indicated period was collected and meanwhile, the same amount of PBS was added. The ATRA release from FD@ATRA was determined by high-performance liquid chromatography (Waters, USA). The release amount of ATRA from FD@ATRA under normoxia was also determined by incubating it in PBS without $Na_2S_2O_4$.

2.10. Cumulative release detection of DAC at different pH conditions

Three equal parts of Ft@DAC solution were taken and placed in PBS with pH of 5.5, 6.8, and 7.4, and the mixed solution was placed in a dialysis bag at 37 °C. The dialysate at indicated times was collected and the DAC content was measured by UV−Vis spectrophotometer (Shimadzu, Japan).

2.11. Cell culture

4T1 cells obtained from American Type Culture Collection (ATCC) were cultured in RPMI-1640 medium containing 10% fetal bovine serum (FBS) in an incubator at 37 °C under 5% CO_2. RAW264.7 purchased from ATCC were cultured in DMEM medium containing 10% FBS at 37 °C under 5% CO_2. CAFs obtained from iCell Bioscience Inc. (China) were cultured in DMEM supplemented with 10% FBS at 37 °C and 5% CO_2 atmosphere.

2.12. Cell uptake of preparations

Firstly, FITC was used instead of DAC to prepare Ft@FITC The specific experimental method for labeling FITC on Ft was as follows: 5.4 mg of Ft was dissolved in 2.0 mL $NaHCO_3$ solution (pH = 9), 6 mg of FITC was dissolved in 2 mL DMSO, and then 500 μL of the prepared FITC solution was dropped into the above protein solution. After the reaction for 12 h, the ammonium chloride (21 mg) was added to terminate the reaction. To study the targeting ability of Ft@DAC to different cells, 4T1 cells, CAFs, and RAW 264.7 cells were cultured in 6-well plates. The medium containing Ft@FITC was incubated with cells for 4 h (the concentration of FITC was 2 μg/mL), and then the cells were washed with PBS buffer twice to remove free drugs, collected, and then re-suspended in 500 μL PBS buffer for flow cytometry detection (BD, USA).

2.13. Detection of cell death

Firstly, 4T1 tumor cells (1×10^5/well) were inoculated in 6-well plates and cultured overnight. The cells were divided into a control group, RT group, Ft@DAC group, and RT + Ft@DAC group, respectively. After the cells were incubated with a drug-containing medium for 8 h (the working concentration of DAC was 2 μg/mL), the medium was discarded and then the cells in RT and RT + Ft@DAC groups were treated with 6 Gy X-ray irradiation. After culture for another 48 h, the cells were collected and stained with Annexin V-FITC and Propidium Iodide for flow cytometry analysis.

2.14. Morphological observation of 4T1 cell death

4T1 cells were cultivated overnight and then divided into a control group, RT group, Ft@DAC group, and RT + Ft@DAC group. After 8 h of co-incubation with different drug-containing media according to the group (the working concentration of DAC was 2 μg/mL), the cells in the RT and RT + Ft@DAC groups were placed under the X-ray irradiator for X-ray irradiation (the irradiation dose was 6 Gy). After another 48 h of culture, the treated cells were observed and recorded under a microscope (Leica, Germany).

2.15. Western blot analysis

Western blot was used to detect the expression of Caspase-3, cleaved Caspase-3, GSDME, and N-GSDME. Specifically, 4T1 cells were cultured in cell culture dishes and incubated with different preparations for 8 h, respectively. Subsequently, cells in the RT and RT + Ft@DAC groups are exposed to 6 Gy irradiation. After 48 h of irradiation, the cells were collected for protein extraction. Anti-DFNA5/GSDME and Caspase-3 (D3R6Y) Rabbit mAb antibodies were applied to detect the expression of relevant proteins.

2.16. LDH, ATP, and IL-1β release detection

4T1 cells were seeded in 6-well plates and cultured overnight, then the cells in Ft@DAC and RT + Ft@DAC groups were incubated with Ft@DAC-containing medium (the working concentration of DAC was 2 μg/mL) for 8 h. Subsequently, the cells in RT and RT + Ft@DAC groups were treated with 6 Gy X-ray irradiation. After another 48 h culture, cells were collected and the release of LDH, ATP, and IL-1β was detected according to the corresponding ELISA detection kits.

2.17. In vitro detection of DC maturation

4T1 tumor cells were inoculated in 6-well plates and cultured overnight. The cells were divided into a control group, Ft@DAC group, RT group, and RT + Ft@DAC group, respectively. After the cells were incubated with a drug-containing medium for 8 h (the working concentration of DAC was 2 μg/mL). The cells in RT and RT + Ft@DAC groups were treated with 6 Gy irradiation. To detect dendritic cells (DCs) maturation, the supernatant of 4T1 cells was carefully collected after culture for another 48 h and then incubated with DCs for 24 h. Subsequently, the DCs were collected and stained with anti-mouse CD86 and anti-mouse CD80 antibodies for flow cytometry analysis.

2.18. *In vivo anti-tumor immune response study*

When the tumor grew to 80 mm^3, tumor-bearing mice with similar body weight were selected and randomly divided into the following five groups, including the Saline group, FD@ATRA group, RT group, RT + FD group, and RT + FD@ATRA group, with three mice in each group. The mice were intravenously injected Saline, FD, and FD@ATRA (equivalent DAC concentration: 6 mg/kg; ATRA concentration: 8 mg/kg), respectively. For the mice in the RT group, RT + FD group, and RT + FD@ATRA group, tumor tissues were irradiated at a dose of 6 Gy at 48 h post-administration and lead blocks were used to protect other parts of the mice. After irradiation for 48 h, the tumor was collected to study the anti-tumor immune response through immunogenic death markers, MDSC infiltration, and $CD8^+$ T cell activation detection, respectively. Meanwhile, lymph nodes were collected to detect the activation status of DCs.

2.19. *In vivo anti-tumor effect study*

2×10^6 4T1 cells re-suspended in 100 μL PBS were subcutaneously injected on the right flank of a healthy BALB/c mouse to establish the primary tumor, and then the same number of 4T1 cells was subcutaneously injected on the left flank of the mouse to construct the distant tumor on Day 5. When the primary tumor grows to 80 mm^3, tumor-bearing mice with similar body weight and good survival status were randomly divided into the following six groups including the Saline group, FD@ATRA group, RT group, RT + FD group, RT + FD@ATRA group, and RT + FD@ATRA+α-PD-L1 group with six mice in each group. The mice were intravenously injected with various preparations (the equivalent concentration of DAC and ATRA were 6 mg/kg and 8 mg/kg), followed by the therapeutic irradiation (6 Gy) at 48 h post-injection for two cycles. The mice in the RT + FD@ATRA+α-PD-L1 group were intraperitoneally injected with α-PD-L1 (5 mg/kg) at 12 h post-irradiation, and the volume of primary and distal tumors were monitored every two days. The tumor was collected and photographed on day 24.

2.20. *Activation of systemic anti-tumor immune response*

After the treatment of the bilateral tumor-bearing mice, the distant tumor was dissociated to obtain the single cell suspension, followed by staining with APC-Cy7 anti-mouse CD8a, APC anti-mouse IFN-γ, and PE anti-mouse Ki67 to study the proliferation and activation of $CD8^+$ T cells in distant tumor tissue. Meanwhile, the mouse spleen was collected and ground to obtain cell suspension for the detection of $CD3^+CD8^+CD44^{high}CD62L^{low}$ effector memory T cells. The blood of mice was collected to detect the pro-inflammatory cytokines of TNF-α, IL-6, and IL-12.

2.21. *Applied to large-volume tumors*

4×10^6 4T1 cells re-suspended in 100 μL PBS were injected subcutaneously into the right flank of healthy BALB/c mice as primary tumors, and then 4×10^6 4T1 cells re-suspended in 100 μL PBS were injected subcutaneously into the left flank of BALB/c mice to establish a distal tumor. When the tumor grew to 300 mm^3, tumor-bearing mice were randomly divided into four groups, including the Saline group, RT group, RT + FD@ATRA group, and RT + FD@ATRA+α-PD-L1 group, with five mice in each group. The mice were intravenously injected with saline and FD@ATRA, and the contents of DAC and ATRA were 6 mg/kg and 8 mg/kg, respectively. For mice in the irradiation group, lead blocks were used to protect other parts, and the right tumor was irradiated (6 Gy) after 48 h of administration. In addition, the mice in the RT + FD@ATRA+α-PD-L1 group were intraperitoneally injected with α-PD-L1 at a dose of 5 mg/kg after 12 h of irradiation. The mice were dissected on the 26th day and the tumor was collected for further analysis.

2.22. *Statistical analysis*

All data are presented as mean ± standard deviation (SD). Statistical analysis was performed using Student's *t*-test. Statistical significance was indicated as $^*P < 0.05$, $^{**}P < 0.01$, $^{***}P < 0.001$ and $^{****}P < 0.0001$.

3. Results

3.1. *Immunosuppression landscape after RT promotes breast cancer progression*

In this study, we first constructed a 4T1 mouse breast cancer model to investigate the anti-tumor efficiency of RT and RT combined with α-PD-L1. The tumor in the RT group was treated with 6 Gy irradiation and the untreated saline group was used as a control. The tumor volumes were monitored every two days to investigate the tumor growth after RT. At the same time, the tumor-bearing mice were also treated with RT combined with α-PD-L1 to investigate the anti-tumor effect of radiotherapy plus PD-L1 blockade. As shown in Fig. 1A−C, we found that the inhibition effect of RT on the late growth stage of the tumor was poor, and the survival time of tumor-bearing mice was not significantly prolonged. Immunofluorescence staining of Ki67 also indicated that RT-treated mice showed similar tumor proliferation properties to the mice in the saline group (Fig. 1J). Moreover, the treatment benefits of RT didn't significantly improve when further combined with α-PD-L1, similar low tumor suppression efficiency and no significant improvement in survival of mice was observed (Fig. 1D−F). The above results collectively indicated that RT had a limited inhibitory effect on tumor growth as reported in some studies[33].

To further explore the reasons and potential mechanisms for RT-induced weak tumor inhibition, the tumor tissue was conducted at 48 h post-RT for transcriptomic analysis. A total of 2733 differentially expressed genes were identified, of which 1461 genes were upregulated and 1272 genes were downregulated after RT (Fig. 1G and Supporting Information Fig. S1). Gene Ontology (GO) and Kyoto Encyclopedia of Genes and Genomes (KEGG) analysis further showed that the differentially expressed genes were significantly enriched in biological processes related to immune functions (Fig. 1H), and some encoding genes related to immunosuppression, mainly including *Cxcl1*, *Vegfa*, and *Ccr2*, were significantly upregulated in the tumor after RT (Fig. 1I). To further study the cellular mechanism of immune landscape induced by RT, we performed immunofluorescence staining and flow cytometry analysis on tumor tissue in saline and RT groups. As shown in Fig. 1J and K, the frequency of tumor-infiltrating $CD45^+$ immune cells significantly increased after RT, with the majority being $CD11b^+$ myeloid cells. Flow cytometry analysis further revealed that $CD11b^+Gr\text{-}1^+$ MDSCs constituted the majority of $CD45^+$ tumor-infiltrating leukocytes in this animal model

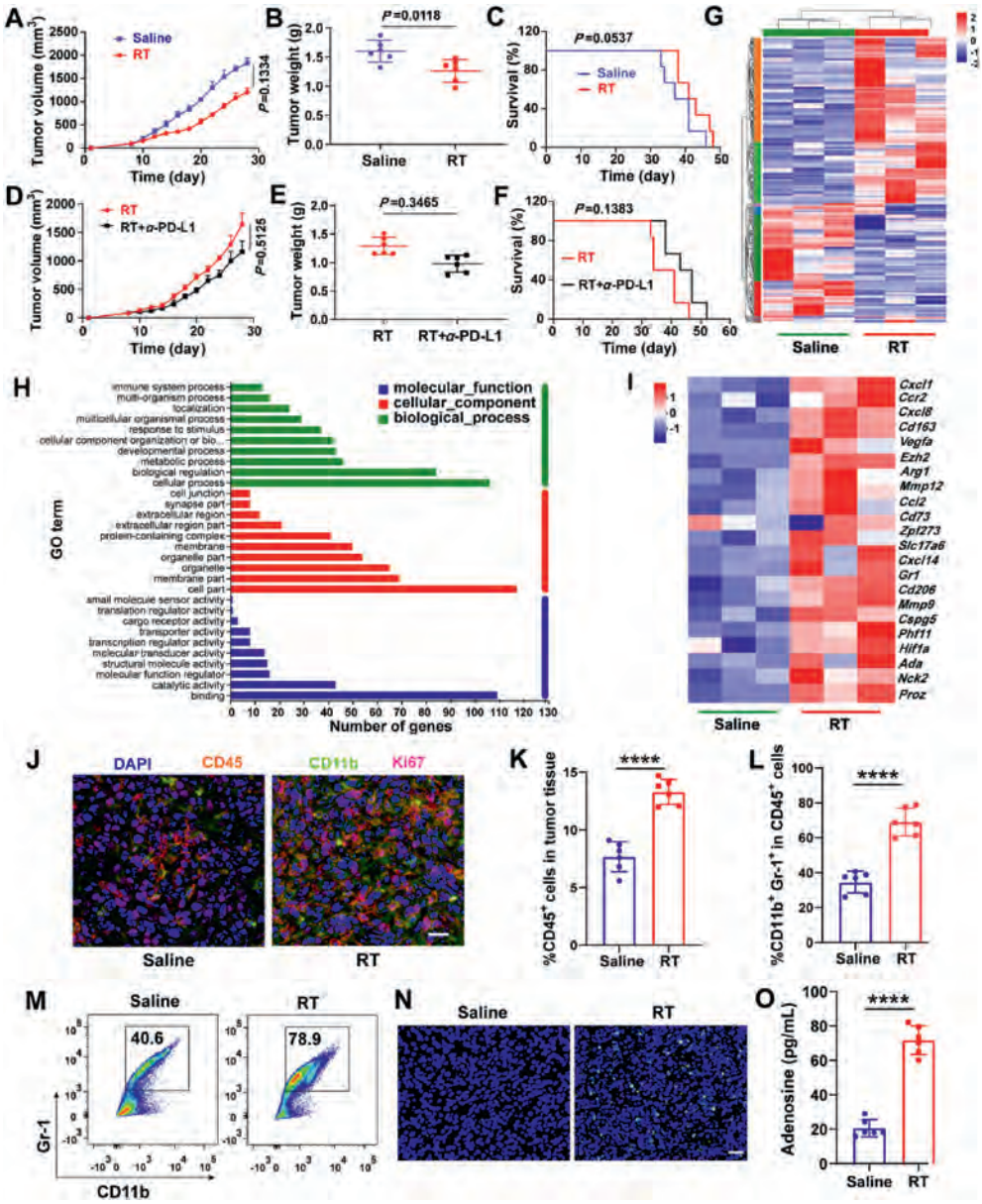

Figure 1 Immunosuppression after radiotherapy promotes breast cancer progression. Tumor growth curves (A) and weights (B) of mice before and after RT ($n = 6$). (C) Survival curve of mice after different treatments ($n = 6$). Tumor growth curves (D) and weights (E) of mice treated with RT and RT plus α-PD-L1 ($n = 6$). (F) Survival curve of mice after different treatments ($n = 6$). (G) Cluster analysis of differential expression genes between untreated and RT-treated tumors 48 h post-RT ($n = 3$). (H) Gene Ontology (GO) analysis of tumor tissues before and after RT (select the top 10 for each item). (I) Heat map of differentially expressed genes related to apoptosis and immune suppression ($n = 3$). (J) Immunofluorescence staining images of tumor tissue in saline and RT groups (scale bar = 20 μm). (K) Quantitative analysis of tumor-infiltrating $CD45^+$ cells ($n = 6$). Representative flow cytometry images (M) and quantitative analysis (L) of tumor-infiltrating MDSCs ($n = 6$). (N) The TUNEL staining of tumor section (scale: 25 μm). (O) Adenosine content detection in tumor tissue ($n = 6$). Data are presented as mean ± SD. ****$P < 0.0001$ determined by Student's t-test.

(Fig. 1L and M), and the frequency of tumor-infiltrating MDSCs significantly increased by 38.3% post-RT. MDSCs are immature myeloid cells, they can promote tumor immune evasion through a variety of mechanisms, including nutrient depletion and secreting anti-inflammatory cytokines, to inactivate cytotoxic T cells and promote tumor growth[34,35].

Additionally, we also found that some encoding genes related to apoptosis, including *Ada* and *Nck2*, were upregulated in tumor tissue after RT (Fig. 1I), and TUNEL staining showed that the tumor underwent apoptosis (Fig. 1N). Moreover, adenosine, the signaling substance related to apoptosis[36-38], was detected in tumor tissue after RT, which was 3.5-fold higher than that in the saline group (Fig. 1O). The apoptotic tumor cells help to establish an immunosuppressive tumor microenvironment by evading immune monitoring, thereby the current tumor treatment strategies primarily focused on inducing tumor apoptosis (*e.g.*, chemotherapy) are less satisfactory in eliciting antitumor immunity[39].

Collectively, the above results demonstrated that RT created an immunosuppressive tumor landscape characterized by recruiting a large number of MDSCs and inducing immunologically silent tumor apoptosis, thus hindering the efficacy of RT and RT in combination with PD-L1 blockade therapy.

3.2. Synthesis and characterization of FD@ATRA immunomodulator

Based on the underlying immunosuppressive principles responsible for RT, we developed an immunostimulant nanomedicine in this study to remodel the immunosuppressive TME post-RT for enhanced radioimmunotherapy. ATRA, an agent that can promote the differentiation of MDSCs into inflammatory macrophages[40,41], was applied to efficiently eliminate MDSCs-mediated immunosuppression. Here, a ferritin (Ft)-based nanomedicine was constructed for tumor-targeted DAC delivery and TME-triggered ATRA release, increasing tumor immunogenicity by reversing tumor apoptosis to immunogenic pyroptosis[42,43] and meanwhile relieving immunosuppressive microenvironment to synergistically promote $CD8^+$ T cells activation. First, DAC, the DNA methylase inhibitor, was encapsulated in Ft nanocages using a temperature regulation method (denoted as Ft@DAC). Transmission electron microscopy (TEM) image showed that Ft@DAC had a spherical structure with a diameter of approximately 20 nm (Fig. 2A), the successful loading of DAC was verified by UV−vis spectrum and Zeta potential change (Fig. 2B and Supporting Information Fig. S2A). Then, the hypoxia reactive azobenzene-4,4-dicarboxylic acid (AZO) was applied to cross-link Ft@DAC by amide bond, and meanwhile, ATRA was encapsulated to obtain Ft@DAC@ATRA nano assembly (denoted as FD@ATRA). TEM and dynamic light scattering (DLS) results revealed that the average particle size of FD@ATRA increased to about 190 nm after crosslinking (Fig. 2A and Fig. S2B). Compared with FD nanoassembly without ATRA, the characteristic absorption peak of ATRA at 335 nm appeared in the UV−Vis spectrum of FD@ATRA, further confirming the successful loading of ATRA (Fig. 2C). And the quantitative analysis results demonstrated that the loading efficiency of DAC and ATRA in FD@ATRA was 17.8% and 22.3%, respectively (Fig. 2D). In addition, the DLS and Zeta potential of FD@ATRA didn't significantly change within one week in various solutions, including PBS, RPMI-1640, and 10% fetal bovine serum (FBS), indicating its excellent stability (Supporting Information Fig. S3). Moreover, the hemolysis rate was below 5% when the concentration of FD@ATRA reached 100 μg/mL, and FD@ATRA showed no obvious cytotoxicity to normal cells, indicating its good biosafety *in vitro* (Supporting Information Fig. S4).

Subsequently, FD@ATRA was treated with sodium dithionite ($Na_2S_2O_4$), a chemical mimic of the hypoxia biomarker

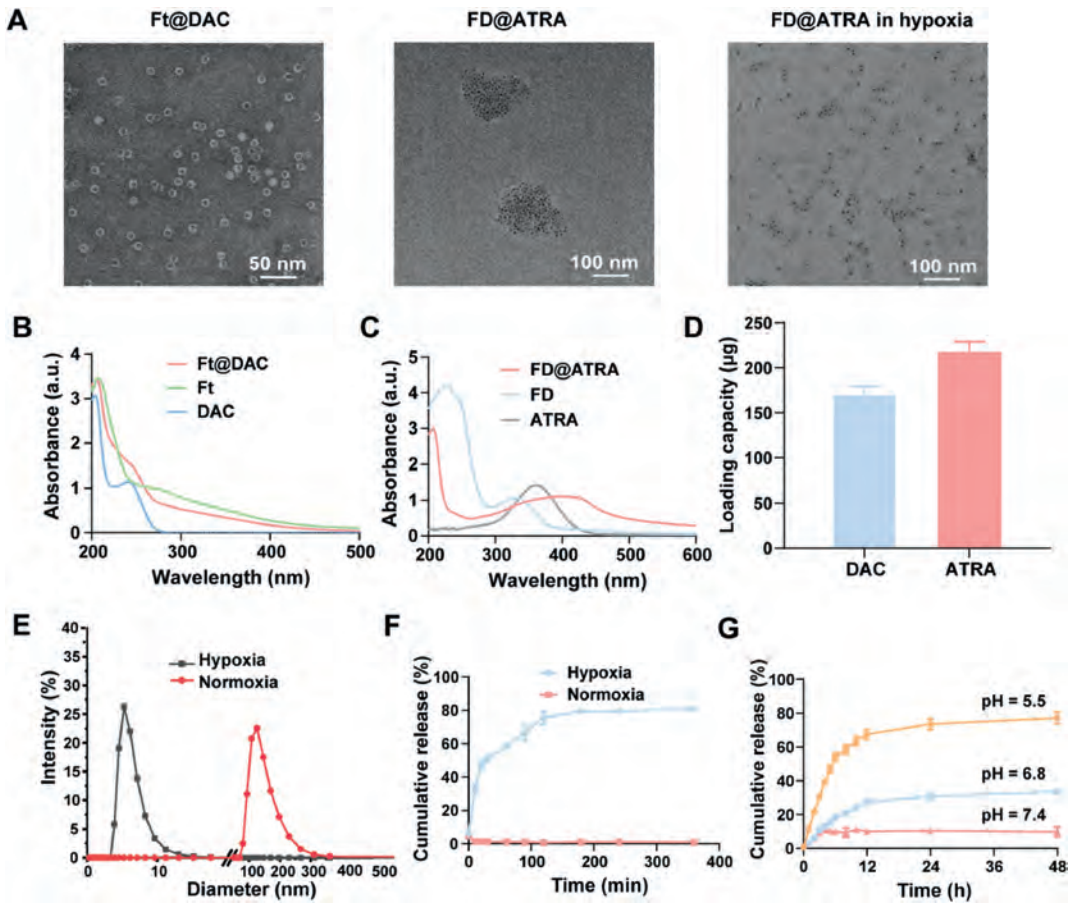

Figure 2 Synthesis and characterization of FD@ATRA nanomedicine. (A) TEM images of various preparations. (B) UV−vis spectrums of DAC, Ft, and Ft@DAC. (C) UV−vis spectrums of ATRA, FD, and FD@ATRA. (D) The loading amount of DAC and ATRA in 1 mg of FD@ATRA ($n = 3$). (E) Hydrate particle size of FD@ATRA under normoxic and hypoxic conditions. (F) ATRA release curves from FD@ATRA under different conditions ($n = 3$). (G) DAC release curves from Ft@DAC in different acidic environments ($n = 3$). Data are presented as mean ± SD.

azoreductase[44], to study the hypoxia responsiveness feature of FD@ATRA. As shown in Fig. 2A and E, the morphology of FD@ATRA was disrupted, and its particle size was reduced from 190 to 22 nm after hypoxia treatment. Meanwhile, the ATRA release was examined by high performance liquid chromatography (HPLC). As displayed in Fig. 2F, negligible ATRA release was observed under normoxia; while the release amount of ATRA dramatically increased to approximately 80% after co-incubation with $Na_2S_2O_4$, suggesting the hypoxia-responsive ATRA release behavior of FD@ATRA. Then, we simulated the acidic environment of tumor lysosomes to investigate the DAC release characteristic of Ft@DAC. As shown in Fig. 2G, Ft@DAC presented a pH-dependent drug release characteristic and the release rate of DAC reached 77% at pH 5.5, which is mainly due to the reversible disassembly of ferritin in the acidic environment[45,46].

3.3. RT combined Ft@DAC induced immunogenic pyroptosis of tumor cells

Next, we used fluorescein FITC instead of DAC to investigate the targeting ability of Ft@DAC to different cells. As shown in Supporting Information Fig. S5A, compared to CAF fibroblast cells and RAW264.7 macrophage cells, the 4T1 tumor cells exhibited a stronger uptake capacity for the formulation. Moreover, we found that compared to free FITC and BSA-based nanopreparation, 4T1 cells had higher uptake efficiency for Ft@FITC (Fig. S5B), suggesting that Ft@DAC could specifically target tumor cells *via* the highly expressed transferrin receptor 1[47]. The mortality rate of 4T1 tumor cells treated with RT or RT-combined Ft@DAC therapy significantly improved compared with the control group (Supporting Information Fig. S6). Next, we further examined the cell death mode of 4T1 cells after various treatments. As displayed in the microscope images (Fig. 3A), RT-treated 4T1 tumor cells displayed cell membrane shriveling and apoptotic bodies producing, while cell swelling with bubbles was observed in 4T1 cells treated with RT + Ft@DAC. Moreover, the pyroptosis-related GSDME protein content in 4T1 cells was significantly increased after Ft@DAC treatment, which was mainly due to DAC-mediated demethylation of the *DFNA5* gene and up-regulated GEDME expression[48]. However, when 4T1 cells were treated with radiotherapy combined with Ft@DAC, the full-length GSDME decreased and the expression of N-GSDME was accordingly increased. And the N-GSDME content was increased by 2.2-fold compared to the individual RT group, indicating that the cleaved Caspase-3 activated by RT could cleave its downstream GSDME substrate and induced pyroptosis (Fig. 3B). Moreover, compared to the RT group, the release of lactate dehydrogenase (LDH, an indication of pyroptotic cell cytotoxicity), adenosine triphosphate (ATP), and IL-1β in the cell supernatant of RT + Ft@DAC group was increased by 1.6-, 1.2-, and 1.4-fold, respectively (Fig. 3C), confirming that Ft@DAC-mediated apoptosis to pyroptosis conversion of tumor cells could release some pro-inflammatory factors. Flow cytometry analysis showed that the frequency of mature dendritic cells (DCs) was significantly increased after RT in combination with Ft@DAC (Fig. 3D), indicating that Ft@DAC-induced pyroptosis enhanced tumor immunogenicity.

3.4. RT combined FD@ATRA activates in vivo immune response

Subsequently, the *in vivo* behavior of FD@ATRA was studied. Its circulation half-life was calculated to be 9.41 ± 1.23 h (Supporting Information Fig. S7A). The fluorescence imaging showed that, compared with free Cy5, Cy5-labeled FD@ATRA could effectively accumulate in the tumor tissue (Fig. S7B and S7C). Encouraged by the superior *in vivo* tumor-targeting performance of FD@ATRA, we further investigated its immunomodulation function and meanwhile chose FD nanoassembly without ATRA as a control. A 4T1 tumor-bearing mouse model was constructed, and the mice were intravenously administered FD@ATRA when the tumor volume grew to 80 mm^3. At 48 h post-injection, the tumors in RT groups were treated with 6 Gy irradiation and then collected at 48 h post-RT. As expected, compared to RT-mediated tumor apoptosis, RT + FD@ATRA-induced pyroptosis promoted more calreticulin (CRT) exposure on the tumor surface, meanwhile accompanied by the increased high mobility group box 1 (HMGB1) protein release (Fig. 4A), indicating the effective activation of immunogenic cell death. Next, we investigated the effect of FD@ATRA on tumor-infiltrating MDSCs after radiotherapy by flow cytometry. As shown in Fig. 4B, the number of MDSCs in tumor tissue significantly increases after RT, while when RT is combined with FD@ATRA treatment, the frequency of tumor-infiltrating $CD11b^+Gr\text{-}1^+$ MDSCs cells significantly decreased by 26.8% compared to the individual RT group, indicating that FD@ATRA could effectively eliminate immunosuppressive MDSCs recruited by RT. Subsequently, the activation and proliferation of $CD8^+$ T cells in tumor tissues after different treatments were further investigated. Representative flow cytometry images and the quantitative analysis results showed that compared with the RT group alone, the frequency of tumor-infiltrating IFN-γ^+CD8^+ T cells and $Ki67^+CD8^+$ T cells in RT+FD@ATRA group increased by 16.8% and 19.4%, respectively (Fig. 4C and Supporting Information Fig. S8). Moreover, FD@ATRA promoted the DCs maturation in the lymph nodes (Fig. 4D). Meanwhile, the quantitative results of flow cytometry are presented in Fig. 4E−G. The above experimental results suggested that FD@ATRA effectively activated immune responses through DAC mediated tumor immunogenic death and ATRA-induced MDSC elimination, remodeling the immune landscape post-RT into a powerful immune-promoting microenvironment.

3.5. RT combined FD@ATRA exhibits excellent antitumor effect and sensitizes PD-L1 blockade therapy

Activating the immune response can promote distal tumor regression, thus we constructed a bilateral 4T1 tumor model to investigate the anti-tumor effect of RT combined FD@ATRA on primary and distant tumors. First, 2×10^6 4T1 cells were subcutaneously injected on the right flank of the mouse to establish the primary tumor, and then the same number of 4T1 cells was subcutaneously injected on the left flank of the mouse to construct the distant tumor on Day 5. The mice were intravenously injected with FD@ATRA, followed by therapeutic irradiation (6 Gy) at 48 h post-injection for two cycles. The mice were also intraperitoneally injected α-PD-L1, further studying the susceptibility of RT combined FD@ATRA to immune checkpoint blockade treatment as illustrated in Fig. 5A. The growth of primary tumors and distant tumors was recorded. Moreover, we found that compared to the RT treatment, the survival time of mice treated with RT + FD@ATRA and RT + FD@ATRA+α-PD-L1 was remarkably extended, and the survival rate increased by 67% (Fig. 5B), indicating that FD@ATRA-mediated immune landscape remodeling could effectively improve the therapeutic benefits of

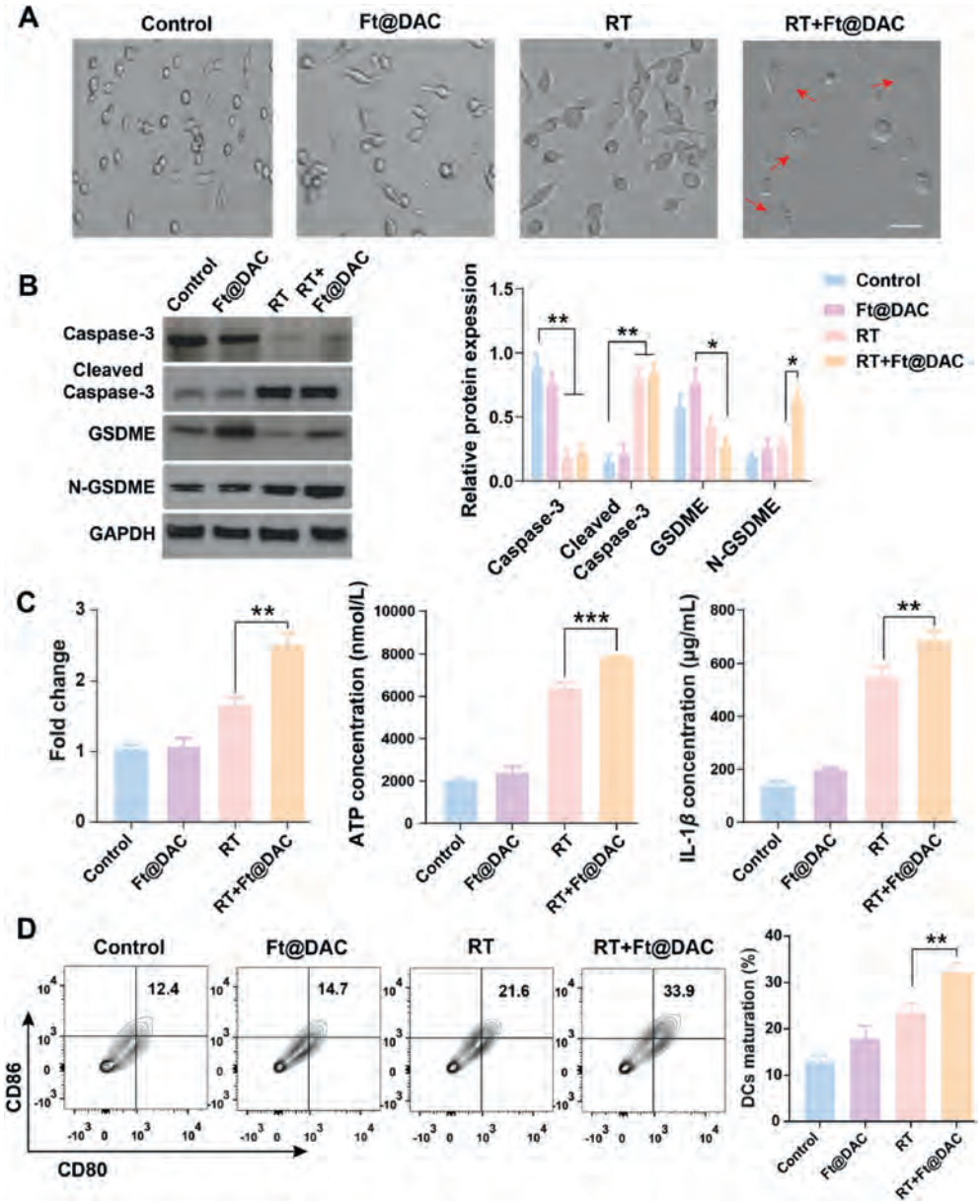

Figure 3 Ft@DAC mediated tumor apoptosis to pyroptosis switch. (A) Microscope images of 4T1 cells after different treatments, scale bar = 30 μm. (B) Western blotting analysis of Caspase-3, cleaved Caspase-3, GSDME, and N-GSDME levels in 4T1 cells after various treatments ($n = 3$). (C) Comparison of LDH, ATP, and IL-1β release in 4T1 cells after different treatments ($n = 3$). (D) Representative flow cytometry images and the quantitative analysis of DCs maturation after different treatments ($n = 3$). Data are presented as mean ± SD. $^*P < 0.05$, $^{**}P < 0.01$, and $^{***}P < 0.001$ determined by Student's t test.

radiotherapy. As displayed in Fig. 5C−F, when RT was combined with FD@ATRA and α-PD-L1 treatments, the anti-tumor effect was significantly enhanced with an excellent tumor inhibition rate of 86%, increased by 32% compared with the mice treated with RT alone. Furthermore, the growth of distant tumors was remarkably inhibited in the RT + FD@ATRA treated mice, with an inhibition rate of 75% against the distant tumor. And the RT + FD@ATRA combined with the PD-L1 treatment group showed the least distant tumor mass and the most significant tumor suppression effect (Fig. 5G−I). The individual tumor growth curves detection also reflected the same result (Fig. 5J), which mainly benefited from the immunomodulatory effects of FD@ATRA. In addition, the H&E staining of tumor tissue collected on day 24 also indicated that the final formulation had the best anti-tumor effects with the most severe histological injury on primary and distant tumors (Supporting Information Fig. S9). Additionally, the biosafety of FD@ATRA was also assessed. There was no significant change in the body weight of mice during monitoring (Supporting Information Fig. S10), and H&E staining indicated that FD@ATRA had no obvious histological damage to the main organs of mice (Supporting Information Fig. S11). Moreover, there was no abnormality in the hematology parameters compared with the saline group (Supporting Information Fig. S12), indicating that FD@ATRA exhibited good biosafety.

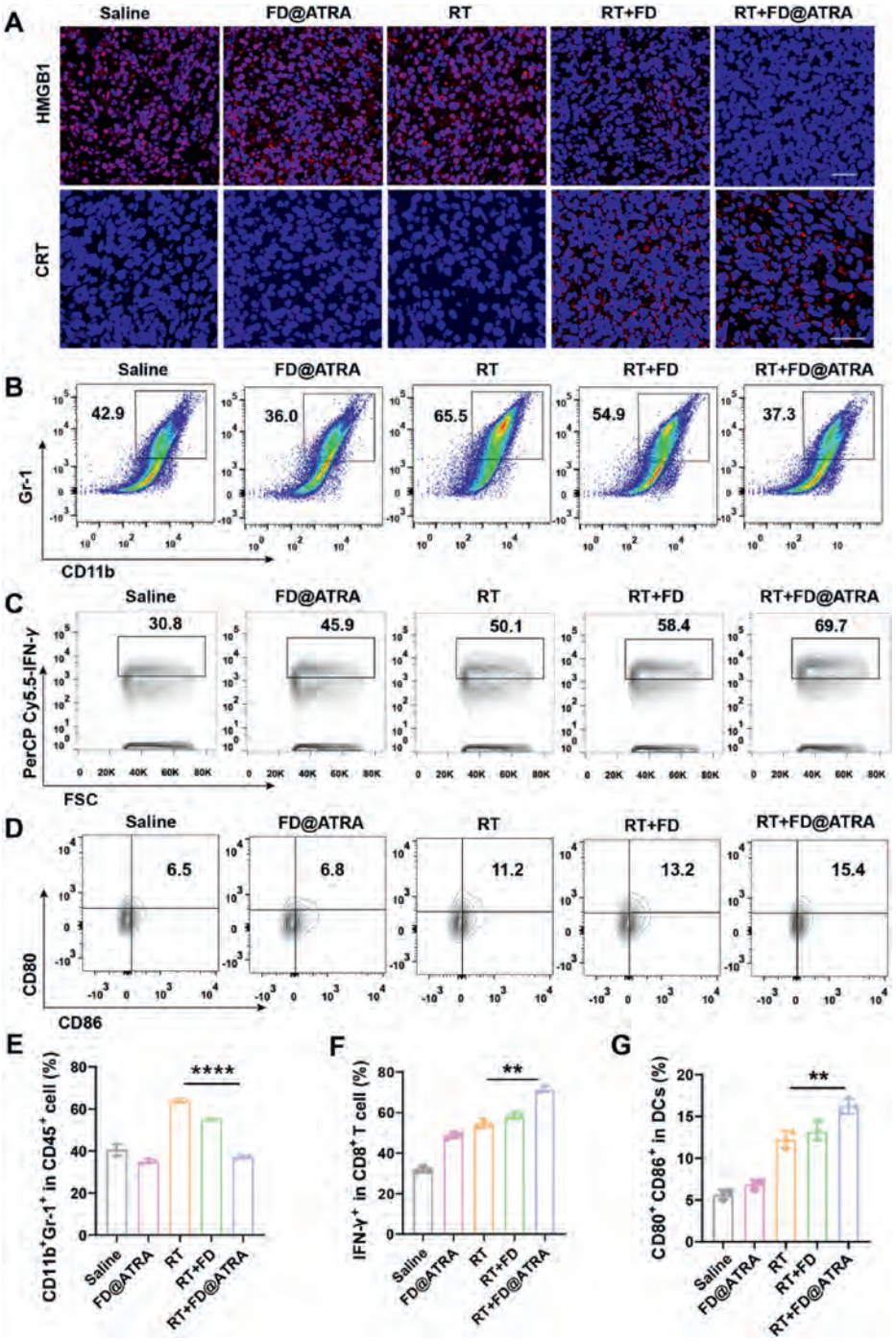

Figure 4 FD@ATRA remodeled the immune landscape after RT. (A) Representative CLSM images of CRT and HMGB1 in tumor tissues of 4T1 tumor-bearing mice receiving different treatments. Red fluorescence: CRT and HMGB1. Scale bars = 50 μm. Representative flow cytometry images (B) and quantitative analysis (E) of MDSCs under different treatments ($n = 3$). Representative flow cytometry images (C) and quantitative analysis (F) of IFN-γ expression on the $CD8^+$ T cells after different treatments ($n = 3$). Representative flow cytometry images (D) and quantitative analysis (G) of the matured DCs in lymph nodes ($n = 3$). Data are presented as mean ± SD. $^{**}P < 0.01$, and $^{****}P < 0.0001$ determined by Student's *t* test.

3.6. Systemic immune activation after FD@ATRA-enhanced RT

We also further analyzed the systemic immune response activation after the treatment cycle. First, the proliferation and activation of $CD8^+$ T cells in distant tumor tissue after various treatments were detected by flow cytometry. As shown in Fig. 6A, compared with individual RT groups, the frequency of activated IFN-γ^+ $CD8^+$ T cells in distant tumor tissue increased after RT in combination with FD@ATRA treatment. Meanwhile, we also observed that the frequency of $Ki67^+$ $CD8^+$ T cells in distant tumor tissue improved by 12% compared to the RT group alone (Fig. 6B). Moreover, after FD@ATRA-enhanced RT treatment, the number of effector

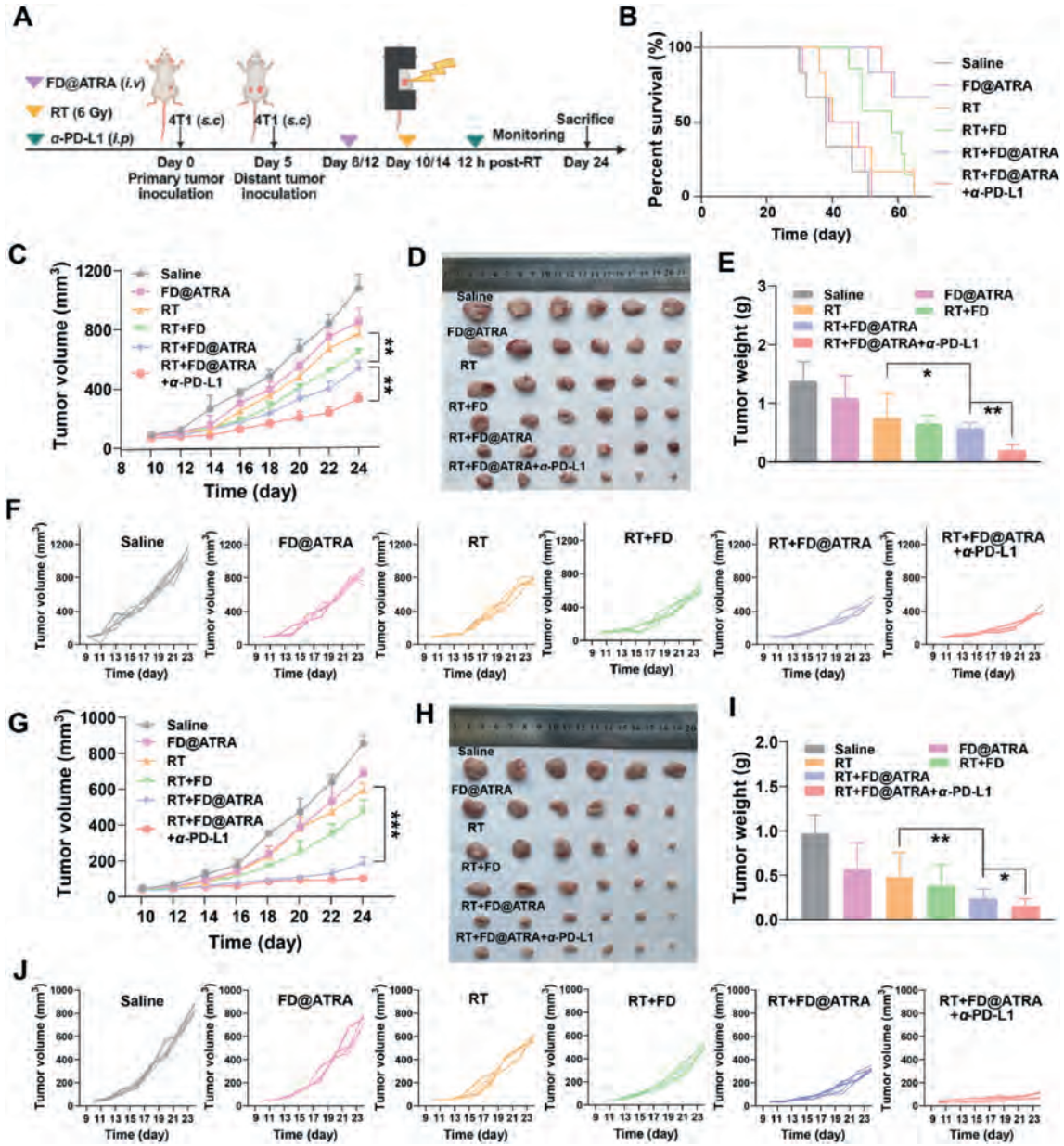

Figure 5 *In vivo* antitumor effect study of RT combined FD@ATRA. (A) Schematic illustration of the treatment schedule to evaluate the antitumor effect of different preparations in a bilateral 4T1 tumor-bearing mouse model. (B) Survival curves of tumor-bearing mice after various treatments ($n = 6$). Primary (C) and distant (G) tumor growth curves of tumor-bearing mice after different treatments ($n = 6$). *In vitro* images of primary (D) and distant (H) tumors were collected from mice on day 24 ($n = 6$). *Ex vivo* primary (E) and distant (I) tumors weight ($n = 6$). Individual growth curves of primary (F) and distant (J) tumors in mice after different treatments ($n = 6$). Data are presented as mean ± SD. $^*P < 0.05$, $^{**}P < 0.01$, and $^{***}P < 0.001$ determined by Student's t-test.

memory T cells in the spleen of mice was 1.9-fold higher than that of RT treatment (Fig. 6C). Fig. 6D−F shows the quantitative results of flow cytometry. We also examined the levels of cytokines in mouse serum after different treatments. As displayed in Fig. 6G, the levels of pro-inflammatory cytokines in the serum of mice, including TNF-α, IL-6, and IL-12, were significantly upregulated after RT + FD@ATRA treatment, which was 1.9-fold, 2.6-fold, and 2.2-fold higher than the RT group, respectively. The above results indicated the effective activation of the system immune response, thus resulting in the effective regression of distant tumors.

3.7. FD@ATRA-enhanced RT combined with α-PD-L1 to treat large-volume tumors

Large tumors often tend to develop complex immunosuppressive landscapes, resulting in immune resistance[49,50]. Thus, we next examined the antitumor effects of FD@ATRA-enhanced RT combined with α-PD-L1 in a 4T1 bilateral tumors model of large-volume (tumor volume >300 mm^3) as illustrated in Fig. 7A. We found that the individual RT group showed slight inhibitions on the growth of distant tumors, in contrast, RT + FD@ATRA+α-PD-L1 could effectively promote distant tumor regression.

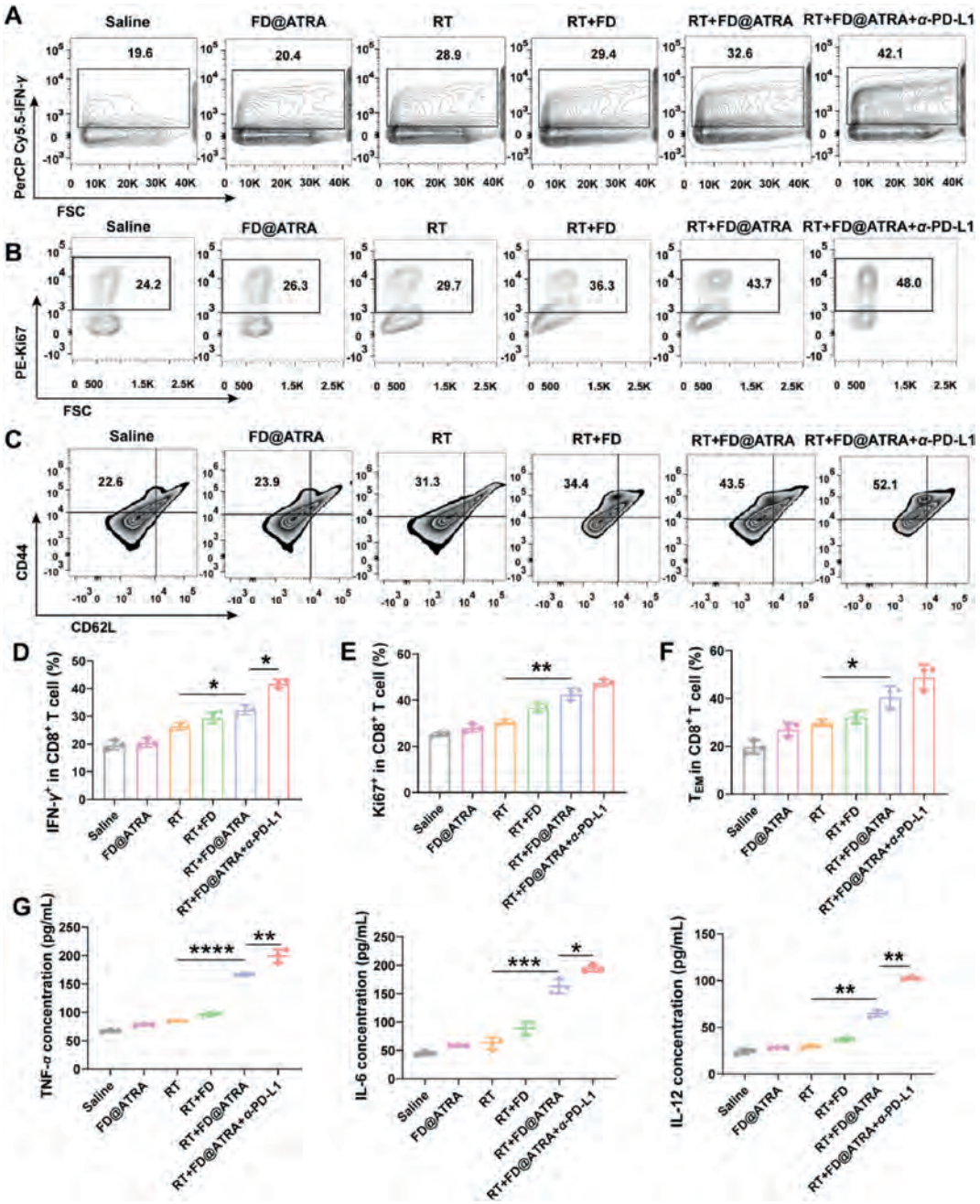

Figure 6 Systemic immune activation after FD@ATRA-enhanced RT. Representative flow cytometry images (A) and quantitative analysis (D) of IFN-γ expression on $CD8^+$ T cells in distant tumors ($n = 3$). Representative flow cytometry images (B) and quantitative analysis (E) of Ki67 expression on the $CD8^+$ T cells in distant tumors ($n = 3$). Representative flow cytometry images (C) and quantitative analysis results (F) of effector memory T cells in the spleen. (G) Cytokine levels of TNF-α, IL-6, and IL-12 in the serum of mice after various treatments ($n = 3$). Data are presented as mean $\pm$ SD. $^*P < 0.05$, $^{**}P < 0.01$, and $^{***}P < 0.001$ determined by Student's t-test.

Compared to the RT group, the inhibition rates of RT + FD@ATRA+α-PD-L1 on distant tumors were increased by 47% (Fig. 7B). The individual growth curves further demonstrated its excellent anti-tumor efficacy on large-volume tumors (Supporting Information Fig. S13). *In vitro* tumor images (Fig. 7C) and tumor weight (Fig. 7D) also exhibited a similar anti-tumor trend. Moreover, immunohistochemistry measurements showed that FD@ATRA combined with RT significantly increased the infiltration of $CD3^+$ and $CD8^+$ T cells in large tumors (Fig. 7E and F), indicating the effective activation of immune response, thereby inducing distant tumor regression. Overall, these results indicated that FD@ATRA-enhanced RT in combination with α-PD-L1 therapy remained effective in large, treatment-resistant tumors and had potent prospects for clinical application.

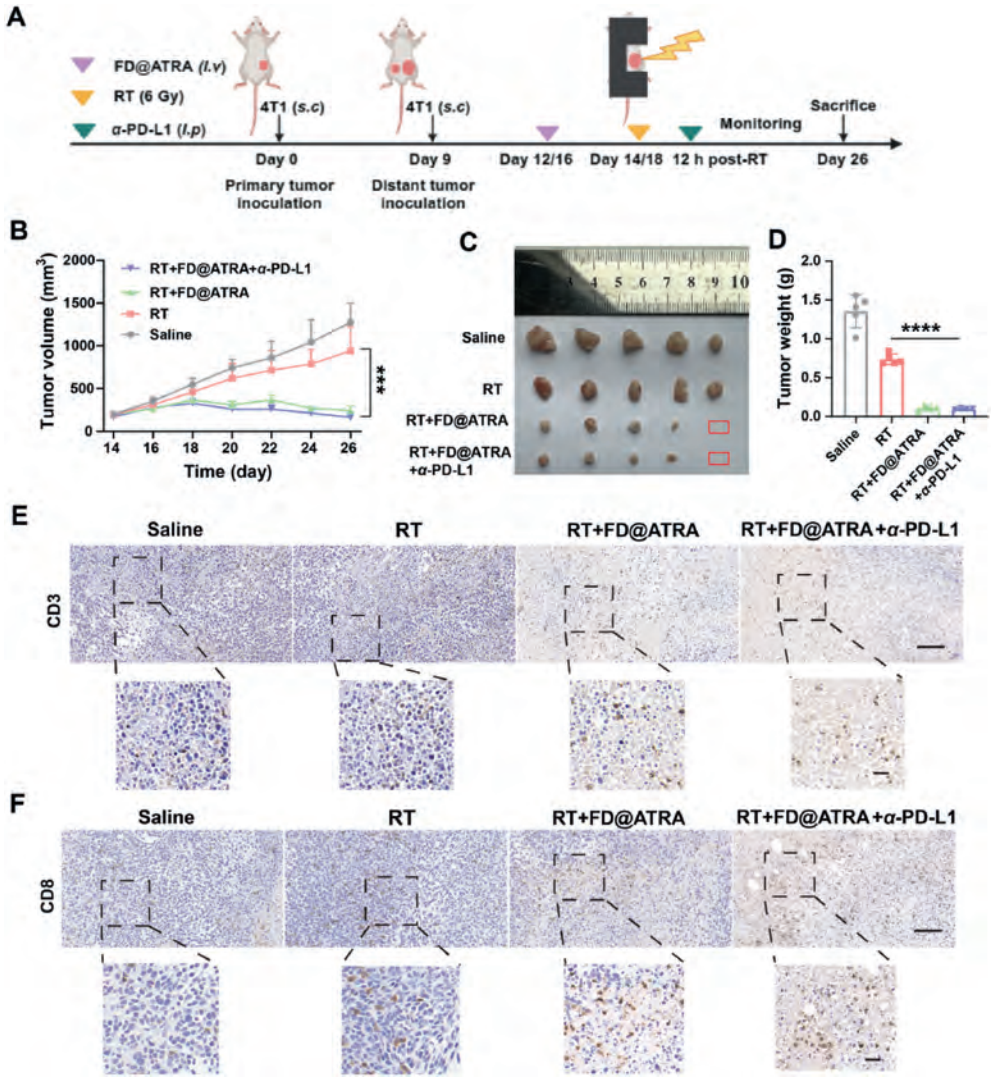

Figure 7 FD@ATRA-enhanced radiotherapy combined with α-PD-L1 to enhance the efficacy of large-volume tumors. (A) Schematic diagram of the therapeutic process for evaluating the anti-tumor effects in a bilateral 4T1 tumor-bearing mouse model of large volume. (B) Distant tumor growth curves of mice after different treatments ($n = 5$). (C) *In vitro* images of the distant tumors ($n = 5$). (D) *In vitro* distant tumors mass ($n = 5$). (E) Immunohistochemical staining of CD3 in tumor tissue slices after different treatments (scale bars = 100 μm). The images below were the corresponding enlarged parts (scale bars = 25 μm). (F) Immunohistochemical staining of CD8 in tumor tissue slices after various treatments (scale bars = 100 μm). The images below were the corresponding enlarged parts (scale bars = 25 μm). Data are presented as mean ± SD. ***$P < 0.001$, and ****$P < 0.0001$ determined by Student's *t*-test.

4. Conclusions

RT serves as the first-line treatment of tumors in the clinic, which can stimulate a systemic immune response by promoting tumor neoantigens generation. However, RT-mediated distal tumor regression is disappointingly rare in clinical practice. Studies have shown that RT could also suppress the activity of cytotoxic T lymphocytes by recruiting some immunosuppressive cells. In this work, the transcriptomic analysis combined with flow cytometry revealed that the genomic landscape shaped by RT created an immunosuppressive milieu by high-influx of immunosuppressive MDSCs, the frequency of tumor-infiltrating MDSCs significantly increased by 37.3% post-RT, and tumor underwent immunologically silent apoptosis after RT treatment. These findings provide a new perspective for understanding the interaction of RT and the immune response, and meanwhile present new targets for developing radio-immunotherapeutic to improve the clinical benefits of RT against solid tumors.

Based on the immunosuppressive milieu shaped by RT, we developed a TME-activated nano assembly (FD@ATRA), which could dissociate in hypoxia TME, enabling spatiotemporally controlled ATRA and DAC delivery to MDSCs and tumor cells, respectively. FD@ATRA cooperatively reprogrammed the immunosuppressive TME post-RT into an immunogenic phenotype by inducing immunogenic pyroptosis of tumor and meanwhile eliminating immunosuppressive MDSCs, resulting in a 16.8% increase in activated $CD8^+$ T cells. Moreover, FD@ATRA combined RT could sensitize the anti-PD-L1 immunotherapy,

resulting in 86% complete regression of distant tumors. Notably, the simple preparation method and mild reaction conditions make FD@ATRA easy to produce on a large scale.

In summary, with an animal experimental model, we found that RT shaped an immunosuppressive landscape characterized by recruiting immunosuppressive MDSCs and meanwhile inducing immunologically silent tumor apoptosis. The developed immunostimulant FD@ATRA could improve the efficacy of RT and RT in combination with PD-L1 blockade therapy. However, several challenges, such as the long-term biosafety of FD@ATRA, and its applicability to other tumors, still require further study for clinical application. Collectively, this work offers a new strategy for improving the clinical benefits of radio-immunotherapy by reshaping the tumor immune landscape after RT.

Acknowledgments

The work was supported by grants from the National Natural Science Foundation of China (Nos. 82172762, 82073395, and 82222067), Outstanding Youth Foundation of Henan Province (No. 222300420020, China), Key Projects of Advantageous Disciplines in Henan Province (No. 222301420011, China), Science and Technology Research Project and Development Plan Joint Fund of Henan Province (No. 232103810059, China), Henan Province Postdoctoral Research Project Initiation Fund (HN2022105, China), Research Start-up Foundation for High-level Talents of Henan University of Technology (No. 2022BS041, China). The authors thank the Modern Analysis and Computing Center of Zhengzhou University for technical assistance.

Author contributions

Mengwan Jiang, Xiu Zhao, and Junjie Liu designed the research. Mingyue Chen carried out the experiments and performed data analysis. Wen Zou and Yingxin Xie participated part of the experiments. Xiu Zhao wrote the manuscript. Junjie Liu revised the manuscript. Mengwan Jiang, Jinjin Shi, Junjie Liu, Aibing Chen, and Xiu Zhao supervised the entire project. All of the authors have read and approved the final manuscript.

Conflicts of interest

The authors have no conflicts of interest to declare.

Appendix A. Supporting information

Supporting information to this article can be found online at https://doi.org/10.1016/j.apsb.2025.11.012.

References

1. Zhen W, Weichselbaum RR, Lin W. Nanoparticle-mediated radiotherapy remodels the tumor microenvironment to enhance antitumor efficacy. *Adv Mater* 2023;**35**:e2206370.
2. Liu J, Liu C, Tang J, Chen Q, Yu Y, Dong Y, et al. Synergistic cerium oxide nanozymes: targeting DNA damage and alleviating tumor hypoxia for improved NSCLC radiotherapy efficiency. *J Nanobiotechnol* 2024;**22**:25.
3. Ling R, Wang J, Fang Y, Yu Y, Su Y, Sun W, et al. HDAC-an important target for improving tumor radiotherapy resistance. *Front Oncol* 2023;**13**:1193637.
4. Luo H, Ma W, Chen Q, Yang Z, Dai Y. Radiotherapy-activated tumor immune microenvironment: realizing radiotherapy-immunity combination therapy strategies. *Nano Today* 2023;**53**:102042.
5. Zhang Y, Sriramaneni RN, Clark PA, Jagodinsky JC, Ye M, Jin W, et al. Multifunctional nanoparticle potentiates the *in situ* vaccination effect of radiation therapy and enhances response to immune checkpoint blockade. *Nat Commun* 2022;**13**:4948.
6. Guo S, Yao Y, Tang Y, Xin Z, Wu D, Ni C, et al. Radiation-induced tumor immune microenvironments and potential targets for combination therapy. *Signal Transduct Targeted Ther* 2023;**8**:205.
7. Mitrea DA, Froicu EM, Prenen H, Gambacorta MA, Span PN, Poortmans P, et al. Combining immunotherapy and radiation therapy in gastrointestinal cancers: a review. *Crit Rev Oncol Hematol* 2024;**199**:104381.
8. Shen M, Guo L, Zhang H, Zheng B, Liu X, Gu J, et al. Differential reinforcement of cGAS−STING pathway-involved immunotherapy by biomineralized bacterial outer membrane-sensitized EBRT and RNT. *J Nanobiotechnol* 2024;**22**:310.
9. Huo M, Wang L, Zhang L, Wei C, Chen Y, Shi J. Photosynthetic tumor oxygenation by photosensitizer-containing Cyanobacteria for enhanced photodynamic therapy. *Angew Chem Int Ed Engl* 2020;**59**:1906−13.
10. Nguyen DM, Phan BN, Reddy SA. Abscopal effect in metastatic melanoma: generating clinical insights from radiation-induced immune response. *Cureus* 2024;**16**:e72853.
11. Marcus D, Lieverse RIY, Klein C, Abdollahi A, Lambin P, Dubois LJ, et al. Charged particle and conventional radiotherapy: current implications as partner for immunotherapy. *Cancers* 2021;**13**:1468.
12. Galluzzi L, Aryankalayil MJ, Coleman CN, Formenti SC. Emerging evidence for adapting radiotherapy to immunotherapy. *Nat Rev Clin Oncol* 2023;**20**:543−57.
13. Qiu J, Xia Y, Bao Y, Cheng J, Liu L, Qian D. Silencing PinX1 enhances radiosensitivity and antitumor-immunity of radiotherapy in non-small cell lung cancer. *J Transl Med* 2024;**22**:228.
14. Karapetyan L, Iheagwara UK, Olson AC, Chmura SJ, Skinner HK, Luke JJ. Radiation dose, schedule, and novel systemic targets for radio-immunotherapy combinations. *J Natl Cancer Inst* 2023;**115**:1278−93.
15. Wang B, Hu J, Zhang J, Zhao L. Radiation therapy regulates TCF-1 to maintain $CD8^+$ T cell stemness and promotes anti-tumor immunotherapy. *Int Immunopharmacol* 2022;**107**:108646.
16. Tuomela K, Mukherjee D, Ambrose AR, Harikrishnan A, Mole H, Hurlstone A, et al. Radiotherapy transiently reduces the sensitivity of cancer cells to lymphocyte cytotoxicity. *Proc Natl Acad Sci U S A* 2022;**119**:e2111900119.
17. Gabrilovich DI, Velders MP, Sotomayor EM, Kast WM. Mechanism of immune dysfunction in cancer mediated by immature $Gr\text{-}1^+$ myeloid cells. *J Immunol* 2001;**166**:5398−406.
18. Jiménez-Cortegana C, Galassi C, Klapp V, Gabrilovich DI, Galluzzi L. Myeloid-derived suppressor cells and radiotherapy. *Cancer Immunol Res* 2022;**10**:545−57.
19. Peng J, Quan DL, Yang G, Wei LT, Yang Z, Dong ZY, et al. Multifunctional nanocomposites utilizing ruthenium (II) complex/-manganese (IV) dioxide nanoparticle for synergistic reinforcing radioimmunotherapy. *J Nanobiotechnol* 2024;**22**:735.
20. Zhang C, Xia D, Liu J, Huo D, Jiang X, Hu Y. Bypassing the immunosuppression of myeloid-derived suppressor cells by reversing tumor hypoxia using a platelet-inspired platform. *Adv Funct Mater* 2020;**30**:2000189.
21. Geng H, Zhou M, Li B, Liu L, Yang X, Wen Y, et al. Metal-drug nanoparticles-mediated osteolytic microenvironment regulation for enhanced radiotherapy of orthotopic osteosarcoma. *Chem Eng J* 2021;**417**:128103.
22. Bian Z, Shi L, Kidder K, Zen K, Garnett-Benson C, Liu Y, et al. Intratumoral SIRPα-deficient macrophages activate tumor antigen-specific cytotoxic T cells under radiotherapy. *Nat Commun* 2021;**12**:3229.
23. Grassberger C, Ellsworth SG, Wilks MQ, Keane FK, Loeffler JS. Assessing the interactions between radiotherapy and antitumour immunity. *Nat Rev Clin Oncol* 2019;**16**:729−45.

24. Lei G, Mao C, Yan Y, Zhuang L, Gan B. Ferroptosis, radiotherapy, and combination therapeutic strategies. *Protein Cell* 2021;**12**: 836−57.
25. Lei G, Zhang Y, Koppula P, Liu X, Zhang J, Lin SH, et al. The role of ferroptosis in ionizing radiation-induced cell death and tumor suppression. *Cell Res* 2020;**30**:146−62.
26. McLaughlin M, Patin EC, Pedersen M, Wilkins A, Dillon MT, Melcher AA, et al. Inflammatory microenvironment remodelling by tumour cells after radiotherapy. *Nat Rev Cancer* 2020;**20**:203−17.
27. Petroni G, Cantley LC, Santambrogio L, Formenti SC, Galluzzi L. Radiotherapy as a tool to elicit clinically actionable signalling pathways in cancer. *Nat Rev Clin Oncol* 2021;**19**:114−31.
28. Zhang Z, Liu X, Chen D, Yu J. Radiotherapy combined with immunotherapy: the dawn of cancer treatment. *Signal Transduct Targeted Ther* 2022;**7**:258.
29. Li K, Shi H, Zhang B, Ou X, Ma Q, Chen Y, et al. Myeloid-derived suppressor cells as immunosuppressive regulators and therapeutic targets in cancer. *Signal Transduct Targeted Ther* 2021;**6**:362.
30. Wang L, Dou X, Chen S, Yu X, Huang X, Zhang L, et al. YTHDF2 inhibition potentiates radiotherapy antitumor efficacy. *Cancer Cell* 2023;**41**:1294−308.e8.
31. Ning J, Chen L, Zeng Y, Xiao G, Tian W, Wu Q, et al. The scheme, and regulative mechanism of pyroptosis, ferroptosis, and necroptosis in radiation injury. *Int J Biol Sci* 2024;**20**:1871−83.
32. Wang L, Chen J, Chai Y, Han W, Shen J, Li N, et al. Targeting regulation of the tumour microenvironment induces apoptosis of breast cancer cells by an affinity hemoperfusion adsorbent. *Artif Cells, Nanomed Biotechnol* 2021;**49**:325−34.
33. Rao E, Hou Y, Huang X, Wang L, Wang J, Zheng W, et al. All-trans retinoic acid overcomes solid tumor radioresistance by inducing inflammatory macrophages. *Sci Immunol* 2021;**6**:eaba8426.
34. Hong SM, Lee AY, Kim BJ, Lee JE, Seon SY, Ha YJ, et al. NAMPT-driven M2 polarization of tumor-associated macrophages leads to an immunosuppressive microenvironment in colorectal cancer. *Adv Sci* 2024;**11**:e2303177.
35. Neo SY, Tong L, Chong J, Liu Y, Jing X, Oliveira MMS, et al. Tumor-associated NK cells drive MDSC-mediated tumor immune tolerance through the IL-6/STAT3 axis. *Sci Transl Med* 2024;**747**:eadi2952.
36. Liang L, Yang LL, Wang W, Ji C, Zhang L, Jia Y, et al. Calcium phosphate-reinforced metal−organic frameworks regulate adenosine-mediated immunosuppression. *Adv Mater* 2021;**33**:e2102271.
37. Xiong H, Ma X, Wang X, Su W, Wu L, Zhang T, et al. Inspired epigenetic modulation synergy with adenosine inhibition elicits pyroptosis and potentiates cancer immunotherapy. *Adv Funct Mater* 2021;**31**: 2100007.
38. Yamaguchi H, Maruyama T, Urade Y, Nagata S. Immunosuppression *via* adenosine receptor activation by adenosine monophosphate released from apoptotic cells. *eLife* 2014;**3**:e02172.
39. Wu Y, Wang C, Yan Y, Hao Y, Liu B, Dong Z, et al. Efferocytosis nanoinhibitors to promote secondary necrosis and potentiate the immunogenicity of conventional cancer therapies for improved therapeutic benefits. *ACS Nano* 2023;**17**:18089−102.
40. Li X, Luo X, Chen S, Chen J, Deng X, Zhong J, et al. All-trans retinoic acid inhibits hepatocellular carcinoma progression by targeting myeloid-derived suppressor cells and inhibiting angiogenesis. *Int Immunopharmacol* 2023;**121**:110413.
41. Cuomo F, Ceglie S, Miguel M, Lindman B, Lopez F. Oral delivery of all-trans retinoic acid mediated by liposome carriers. *Colloids Surf B Biointerfaces* 2021;**201**:111655.
42. Xu XY, Zheng JL, Liang N, Zhang X, Shayibai S, Wang ZX, et al. Bioorthogonal/ultrasound activated oncolytic pyroptosis amplifies *in situ* tumor vaccination for boosting antitumor immunity. *ACS Nano* 2024;**18**:9413−30.
43. Zhu Y, Wang X, Feng L. Intermetallics triggering pyroptosis and disulfidptosis in cancer cells promote anti-tumor immunity. *Nat Commun* 2024;**15**:8696.
44. Wang X, Wu M, Zhang X, Li F, Zeng Y, Lin X, et al. Hypoxia-responsive nanoreactors based on self-enhanced photodynamic sensitization and triggered ferroptosis for cancer synergistic therapy. *J Nanobiotechnol* 2021;**19**:204.
45. Wang X, Liu Y, Xue C, Hu Y, Zhao Y, Cai K, et al. A protein-based cGAS−STING nanoagonist enhances T cell-mediated anti-tumor immune responses. *Nat Commun* 2022;**13**:5685.
46. Zuo T, Fang T, Zhang J, Yang J, Xu R, Wang Z, et al. pH-sensitive molecular-switch-containing polymer nanoparticle for breast cancer therapy with ferritinophagy-cascade ferroptosis and tumor immune activation. *Adv Healthcare Mater* 2021;**10**:e2100683.
47. Liu W, Lin Q, Fu Y, Huang S, Guo C, Li L, et al. Target delivering paclitaxel by ferritin heavy chain nanocages for glioma treatment. *J Control Release* 2020;**323**:191−202.
48. Fan JX, Deng RH, Wang H, Liu XH, Wang XN, Qin R, et al. Epigenetics-based tumor cells pyroptosis for enhancing the immunological effect of chemotherapeutic nanocarriers. *Nano Lett* 2019;**19**: 8049−58.
49. Prindle A, Samayoa P, Razinkov I, Danino T, Tsimring LS, Hasty J. A sensing array of radically coupled genetic 'biopixels'. *Nature* 2011; **481**:39−44.
50. Li Y, Shen Z, Chai Z, Zhan Y, Zhang Y, Liu Z, et al. Targeting MS4A4A on tumour-associated macrophages restores $CD8^+$ T-cell-mediated antitumour immunity. *Gut* 2023;**72**:2307−20.